JOURNAL OF COMPUTATIONAL PHYSICS 29, 370–388 (1978)

P-Wave to Rayleigh-Wave Conversion Coefficients for Wedge Corners; Model Experiments

ANTHONY F. GANGI

Department of Geophysics, Texas A&M University, College Station, Texas 77843

AND

ROBERT L. WESSON

Office of Earthquake Studies, U.S. Geological Survey, Reston, Virginia 22092

Received February 24, 1978

An analytic solution is not available for the diffraction of elastic waves by wedges; however, numerical solutions of finite-difference type are available for selected wedge angles. The *P*- to Rayleigh-wave conversion coefficients at wedge tips have been measured on two-dimensional seismic models for stress-free wedges with wedge angles, θ_0, of 10, 30, 60, 90 and 120°. The conversion coefficients show two broad peaks and a minimum as a function of the angle between the wedge face and the direction of the incident *P*-wave. The minimum occurs for the *P* wave incident parallel to the wedge face and one maximum is near an incidence angle of 90° to the wedge face. The amplitude of this maximum, relative to the other, decreases as the wedge angle increases. The asymmetry of the conversion coefficients, $C_{PR}(\theta; \theta_0)$, relative to parallel incidence ($\theta = 0$) increases as the wedge angle increases. The locations of the maxima and the minimum as well as the asymmetry can be explained qualitatively. The conversion coefficients are measured with an accuracy of $\pm 5\%$ in those regions where there are no interfering waves. A comparison of the data for the 10° wedge with the theoretical results for a half plane (0° wedge) shows good correlation.

INTRODUCTION

The theoretical problems of the diffraction of elastic waves by stress-free or rigid wedges of arbitrary wedge angle are still among the classical unsolved problems in elastodynamics. Only two special cases have been solved. The case of the stress-free "wedge" with 180° wedge angle (the half-space problem) has been solved by Lamb [1] and the cases of stress-free and rigid wedges with 0° wedge angle (diffraction by half-planes) have been solved by Fridman [2, 3], Maue [4], Roseau [5, 6], de Hoop [7], and Miles [8]. These special cases are two limiting cases and must be contained in the solution for a wedge of arbitrary wedge angle.

Some success has been achieved in explaining some of the features of wedge problems by approximate solutions. These deal primarily with the reflection and transmission

0021-9991/78/0293-0370$02.00/0

coefficients of Rayleigh waves at wedge corners. Lapwood [9] used an iterative method to obtain an approxmate expression for the transmission of a Rayleigh pulse around a corner (270° wedge). This technique was extended to higher order by Viswanathan *et al.* [10] to achieve better correlation of theory and experiment. Kane and Spence [11] and Hudson and Knopoff [12] obtained similar first-order approximations for arbitrary wedge angles while using different approaches. Mal and Knopoff [13] extended the latter work to a higher-order approximation and achieved a better correlation of theory and experiment. McGarr and Alsop [14] used an approximate variational method to determine the transmission of Rayleigh waves past a step discontinuity and across the interface between two welded quarter spaces of different elastic properties. They also performed modeling experiments to test their analytic results.

More recently, numerical solutions to wedge problems have been obtained by finite-difference techniques applied to the elastodynamic differential equations and the boundary and initial conditions. Alterman and Rotenberg [15] treated the problem of elastic waves in a stress-free quarter space (i.e., a wedge of 270°) with the source located along the bisector of the wedge angle. The latter condition increases the symmetry of the problem and lessens the demands on computer memory to achieve the solution. Alterman and Lowenthal [16] treated both the quarter space (270° wedge) and three-quarter space (90° wedge) by finite-difference methods. The numerical solutions are given as plots of the displacements as functions of time at various points in the elastic medium and on the wedge faces. Ottaviani [17] obtained numerical solutions by the finite-difference method for the quarter space, again with the source along the diagonal, and for welded quarter spaces. He also performed model studies to compare the numerical results with experiments. Musasinghe and Farnell [18] obtained numerical solutions for a quarter space and a step discontinuity on a surface and extended the results of McGarr and Alsop [14]. They also compare their results for the step discontinuity with the approximate analytic solutions of Mal and Knopoff [19].

The reflection and transmission coefficients for Rayleigh waves have been measured experimentally using seismic models by De Bremaecker [20], Victorov [21], Knopoff and Gangi [22], Gangi [23], and Pilant, *et al.* [24]. In the latter reference both the amplitudes and the phases of these coefficients were measured. In addition, photoelastic studies of wave propagation in a quarter space have been made by Lewis and Dally [25] and Henzi and Dally [26]. The case of a step discontinuity was investigated photoelastically by Dally and Lewis [27]. The advantage of this method is that the stresses in the complete elastic medium can be determined. The disadvantage is that the data reduction process is lengthy in that it requires that interference fringes be counted and measured to determine stresses. Also, there are few materials that have the necessary stress-dependent birefringence. However, it gives a wealth of data from a single experiment when the data are reduced and these data can be compared with the results of the numerical (finite-difference) methods. The amplitudes of the waves diffracted by the wedge tip and faces have been measured by Gangi [23, 28] and Wesson [29]. In particular, the conversion coefficient for *P* waves converted to Rayleigh waves at the wedge tip have been measured for wedge angles of 60 and 90°

[28] and for wedge angles of 10, 30, 60, 90, and 120° [29]. These latter results have been reanalyzed and are reported here to provide additional data as check points for numerical and theoretical calculations.

Experimental Results

The data were obtained using the standard "two-dimensional" seismic-modeling technique [30]. Circles 30 cm in diameter were cut from 1.6-mm (1/16-in.) thick aluminum sheets and wedges of 10, 30, 60, 90, and 180° were cut out of the circles (see Fig. 1). This geometry provides a convenient shape both for the acquisition and reduction of the data. The measured (thin-plate) velocities were: 5.55 $\pm$ 0.05 km/sec for the P waves, 3.27 $\pm$ 0.05 km/sec for the S waves and 2.99 $\pm$ 0.05 km/sec for the Rayleigh waves. These velocities correspond to a "two-dimensional" Poisson's ratio of 0.245. The source transducer was placed on the circular edge of the model and a receiving transducer was fixed on the upper wedge face as shown in Fig. 1. The source transducer was vertically polarized and gives rise to predominantly radial displacements. The receiving transducer was also vertically polarized and measured displacements normal to the wedge surface. The receiving transducer was placed at point "a" which is approximately half way between the wedge corner and the end of the wedge face (e in Fig. 1), that is, $a \simeq \frac{1}{2}r$.

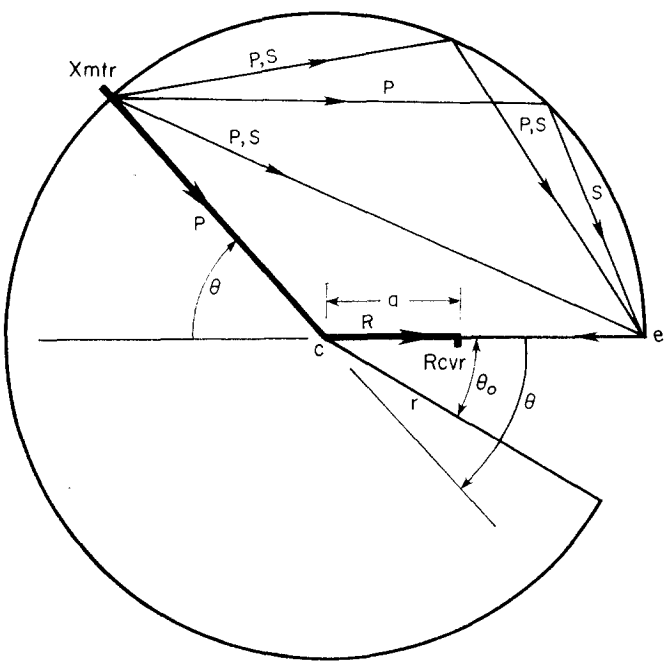

Fig. 1. The seismic model.

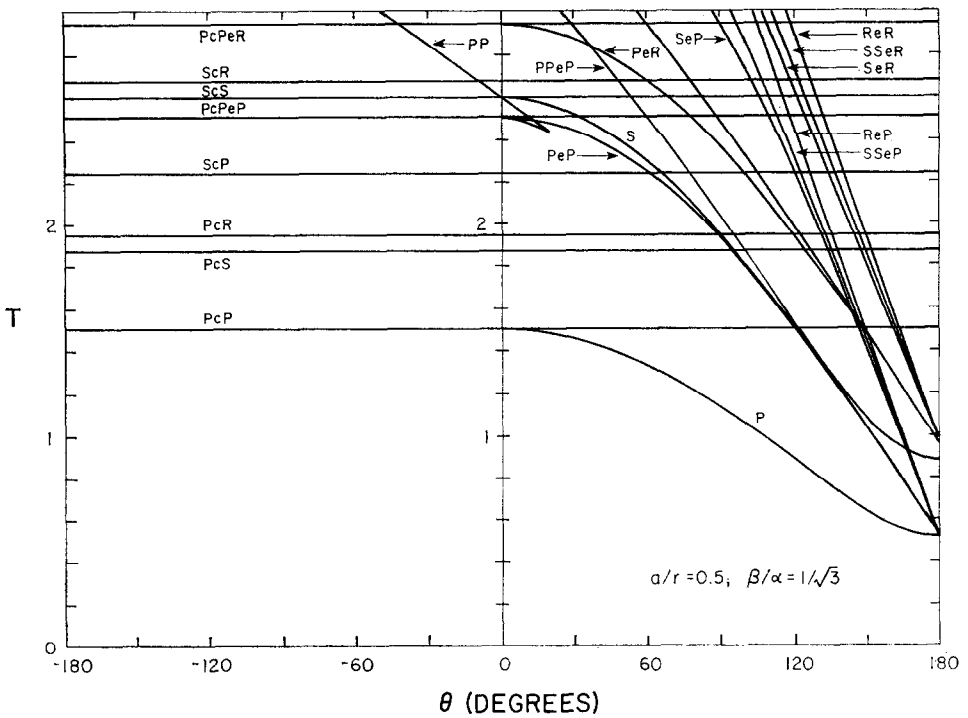

FIG. 2. Travel-time curves for the seismic model; the source on the circular periphery and the receiver on the wedge face at $a/r = 0.5$ for $\beta/\alpha = 3^{-1/2}$, $\sigma = \frac{1}{4}$.

With this geometry, the *P* wave converted into a Rayleigh wave at the wedge corner (*c* in Fig. 1) has the same travel time to the receiver for the source anywhere on the circular edge. There are a large number of possible waves in this model and their travel times are plotted in Fig. 2. The notation used to identify the waves is similar to that used previously [28] where *P* and *S* represent direct body waves from the source to the receiver, *PP* and *SS* represent waves reflected from the curved surface and detected at the receiver, *PS* is the *P* wave converted into an *S* wave at the curved surface, while *PcP*, *PcS*, *PcR* are waves, converted at the wedge corner, which travel along the wedge face to the receiver and are due to an incident *P* wave. *ScP*, *ScS*, and *ScR* are the waves converted at the wedge corner due to an *S* wave from the source. *PeP*, *PeS*, *PeR* represent waves generated at the end of the wedge face (point *e* in Fig. 1) due to a direct *P* wave from the source. The other waves are labeled consistent with this convention; for example, the wave labelled *PcPeP* is the wave that travels as a *P* wave (*P*) from the source to the wedge corner (*c*), is "converted" into a *P* wave which travels along the upper wedge face to its end (*e*) and returns as a *P* wave along the wedge face from the end (*e*) to the receiver.

The travel-time curves in Fig. 2 are computed for a Poisson's ratio of 0.25 and for the receiver located at the midpoint of the upper wedge face. From the figure, it is

seen that the event of interest, the *PcR* wave, has no interference from other events for angles of incidence, θ, ranging from $\theta_0 - 180°$ (when the source is at the intersection of the lower wedge face and the circular boundary) to approximately $+90°$ where the waves *PeP* and *S* have arrival times equal to that of *PcR*. The wave *PcS* immediately precedes the *PcR* wave, but its amplitude is small and does not interfere appreciably with *PcR*. The waveform of the *PcR* wave can be closely approximated by the second derivative of a Gaussian wavelet (see Fig. 3) and has its major frequency content between 50 to 300 KHz. The duration of the pulse is about 7 μsec and the time separation between the arrival times of *PcS* and *PcR* is about 4.5 μsec; consequently, the pulses associated with *PcS* and *PcR* are sufficiently well separated so that they can be individually seen. The amplitude of the *PcS* pulse was always well below one-tenth that of the *PcR* pulse and, therefore, does not interfere strongly with the latter.

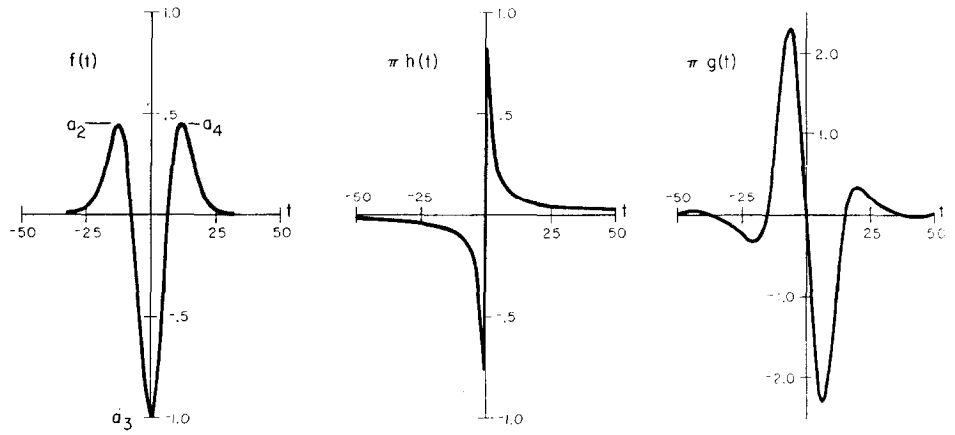

FIG. 3. The assumed input wavelet, $f(t) = [0.02t^2 - 1]\exp(-t^2/100)$, the Hilbert transform of $\pi\delta(t)$, namely $\pi h(t) = 1/t$, and the convolution of $f(t)$ and $\pi h(t)$, $g(t)$; $g(t)$ is the associated function of $f(t)$.

The waveform of *PcR* changes as the angle of incidence of the *P* wave is varied. This occurs because there are two contributions to the *PcR* wave, one is a reproduction of the incident *P*-wave waveform and the other is its *allied function* (or Hilbert transform) [9, 22]. To ameliorate the effects of the waveform change, the "measured" amplitude of the pulse is taken to be the sum of the peak-to-peak amplitudes between the major lobe and the two adjacent minor lobes as shown in Fig. 3; that is, $(a_2 - a_3) + (a_4 - a_3)$.

The results of these measurements for wedge angles, θ_0, of 10, 30, 60, 90, and 120° are given in Fig. 4, 5, 6, 7, and 8 respectively. From the plotted data points, it can be seen that, except for a few points, the scatter is generally less than $\pm 5\%$ in those regions where there is no interference; that is, for angles of incidence, θ, less than $+60°$. The *P*-wave to Rayleigh-wave conversion coefficients have the following

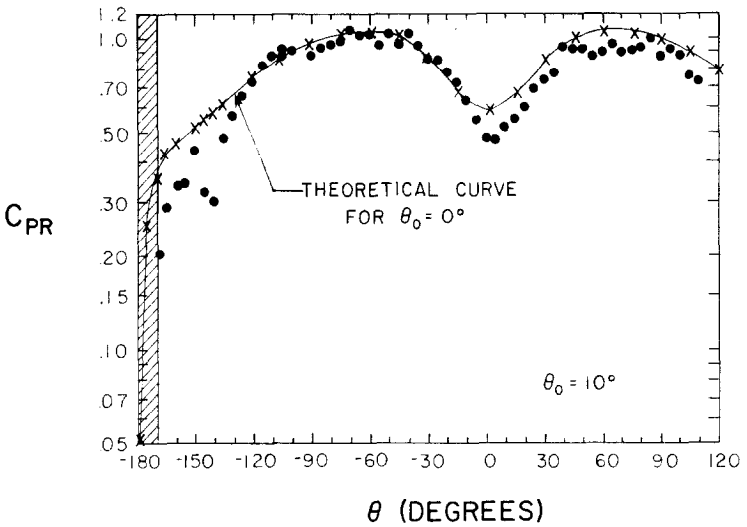

FIG. 4. The measured *P*-wave to Rayleigh-wave conversion coefficient, C_{PR}, for the 10° stress-free wedge and the corresponding theoretical curve for the stress-free, half-plane problem [8].

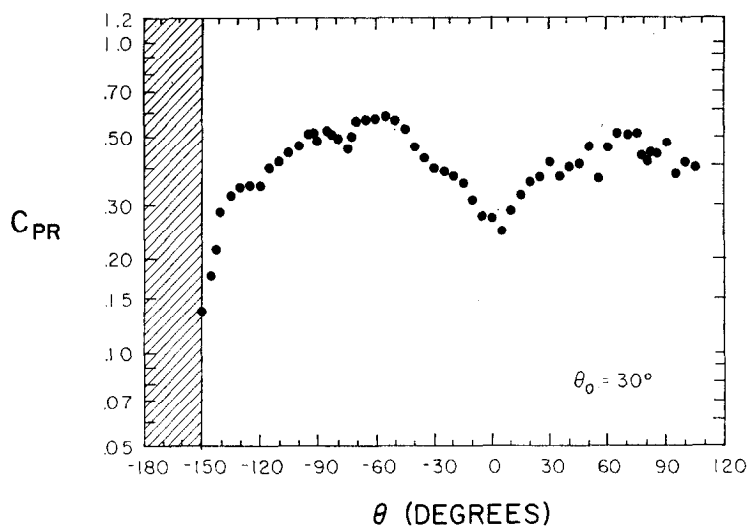

FIG. 5. The measured *P*-wave to Rayleigh wave conversion coefficient, C_{PR}, for the 30° stress-free wedge.

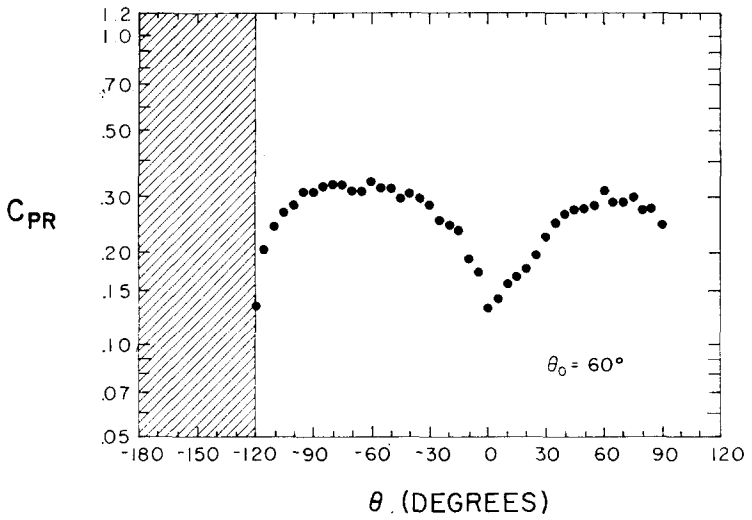

FIG. 6. The measured *P*-wave to Rayleigh wave conversion coefficient, C_{PR}, for the 60° stress-free wedge.

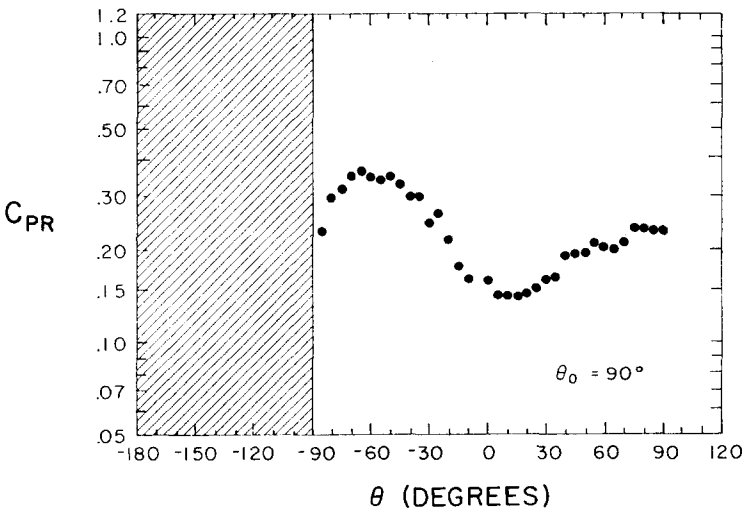

FIG. 7. The measured *P*-wave to Rayleigh wave conversion coefficient, C_{PR}, for the 90° stress-free wedge.

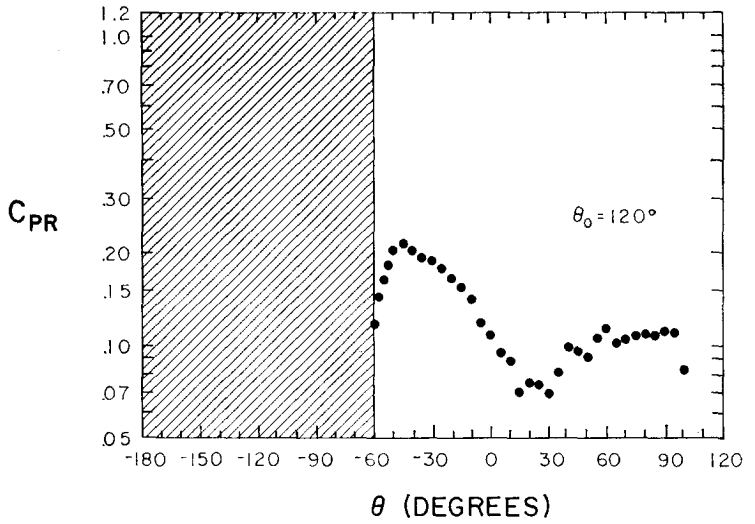

FIG. 8. The measured P-wave to Rayleigh wave conversion coefficient, C_{PR}, for the 120° stress-free wedge.

general characteristics: (i) They show two broad maxima for angles of incidence near $\pm 90°$ and a minimum near 0°. They become small at $\theta_0 - 180°$ and $+180°$; these angles correspond to grazing incidence of the direct P ray on the wedge faces. (ii) The magnitudes of the conversion coefficients decrease as the wedge angle increases. This can be anticipated because the conversion coefficient must go to zero as the wedge angle goes to 180°. (iii) The data are more symmetric about $\theta = 0$ for small wedge angles and the asymmetry increases with increasing wedge angle. The symmetry of the data for small wedge angles ($\theta_0 = 10$ and 30°) is consistent with the theoretical results obtained for the half-plane ($\theta_0 = 0°$) case [2, 3, 4, 5, 6, 7, 8] in which it is shown that the conversion coefficient is exactly symmetric about $\theta = 0°$.

The conversion coefficients shown in Figs. 4 to 8 are normalized with respect to the P-wave amplitude at the wedge corner. This is consistent with the earlier work [28] reported for wedge angles of 60 and 90°. Except in the neighborhood of $\theta = 0°$, the data in Figs. 6 and 7, corresponding to $\theta_0 = 60$ and 90°, are well within 10 % of the values reported earlier [28]. The present data have a sharper and deeper minimum near $\theta = 0°$ for the 60° wedge compared to the broader and shallower minimum of the earlier data. On the other hand, the present data near $\theta = 0°$ for the 90° wedge have a broader and shallower minimum than the earlier data. That is, the character of the minimum for the 60° wedge shown here is very similar to the character of the minimum for the 90° wedge reported earlier. The same holds true for the present data for the 90° wedge and the earlier data for the 60° wedge. This may not be surprising and is probably due to the fact that the amplitudes are smallest in these regions for both wedge angles. In obtaining the data for a particular wedge angle, all gains and signal strengths were held constant throughout the complete range of θ values. The

cuspate behavior for the minimum near $\theta = 0°$ is probably the correct one because that behavior occurs most consistently for the other wedge angles and it is the behavior predicted by the theory for the $\theta_0 = 0°$ wedge or half plane.

The general characteristics of these curves can be explained in terms of a simple physical argument given previously [28]. That is, the minimum near 0° is due to the fact that the *P*-wave motion of the incident wave is radial and the stress-free boundary condition on the upper wedge surface will be satisfied by the incident wave without requiring additional reflected and/or diffracted waves. That there is scattered *P*-, *S*- and *R*-wave energy for $\theta = 0°$ is due to the singularity introduced by the wedge corner. The corner acts as a virtual source and gives rise to the *PcP*, *PcS* and *PcR* waves. On the other hand, the maximum at $\theta = 90°$ would be anticipated because the incident wave is normally incident on the wedge face and a large reaction (in the form of the reflected *P* wave) is induced to satisfy the stress-free boundary condition. Because of the discontinuous nature of the reflected wave and the direct wave near the wedge corner, there will be a large virtual source at the wedge corner. The same consideration would hold for $\theta = -90°$. In addition, large virtual sources at the wedge corner could be anticipated when the wave is normally incident on the lower wedge face, i.e., when $\theta = \theta_0 - 90°$ and $\theta_0 = \theta_0 + 90°$ for the same reason. However, the effect on the upper wedge surface in these cases would probably be smaller than for $\theta = \pm 90°$. The asymmetry in the conversion coefficient about $\theta = 0°$ would be anticipated because of this latter effect.

While the above argument gives some physical feeling for the correctness of the measured conversion coefficients, it does not give quantitative results that can be compared with the measured data. To achieve a quantitative comparison, it is necessary to have theoretical results or finite-difference numerical data.

Comparison of Theory and Experiment

Because analytic solutions to these problems do not exist, it is not possible to make direct comparison of theory and experiment. Comparison with the numerical results is also not possible because: (i) the source locations used in the finite-difference methods do not correspond with the range of locations used in the experiments, (ii) the pulse waveform used in the numerical solutions differs significantly from that obtained experimentally, (iii) insufficient numbers of traces are presented by those using the finite-difference method to make direct comparison possible, and (iv) the 90° wedge case (the three-quarter space case) is the only case treated numerically [16] which corresponds to any of the cases treated here, and that one was computed only for the incidence angle $\theta = -45°$. Our inability to correlate the numerical and experimental data is due, mainly, to the fact that the primary concerns of those performing the numerical analyses were the stability and efficiency of the methods. These are important concerns and it is hoped that, now that the numerical methods have been shown to be stable and efficient, the numerical analysts will treat these problems in more detail so that comparisons can be made with the experimental data.

While none of the cases reported here has been treated analytically, an approximate comparison can be made between the theoretical results for the half-plane problem (0° wedge) and the experimental data for the 10° wedge. We are encouraged to make the comparison because, as previously noted, these data show the symmetry predicted by the analytical results.

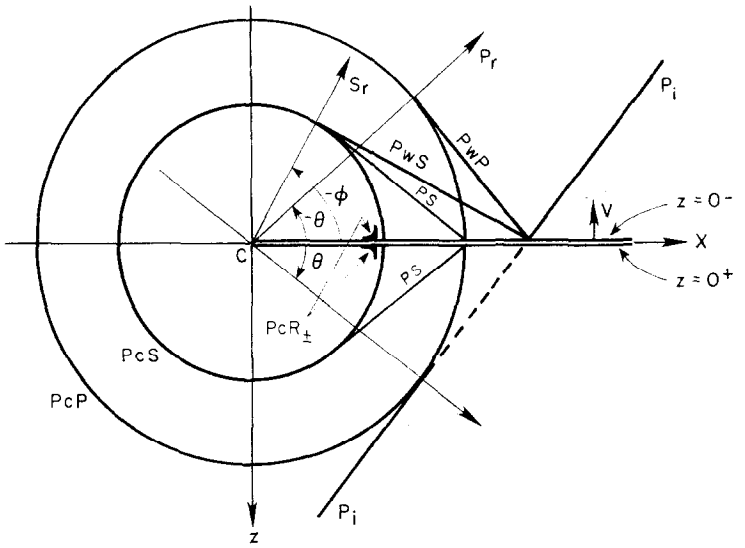

FIG. 9. The geometry and waves (and rays) for the problem of diffraction of a plane *P* wave by a stress-free half plane.

Both de Hoop [7] and Miles [8] give theoretical expressions for the displacements on the wedge faces (as well as everywhere in the medium) for the case of a unit amplitude, plane *P* wave (with delta-function time dependence) incident on the half-plane edge at an arbitrary angle θ at time $t = 0$ (see Fig. 9). We use Miles' notation because his paper is more readily available. Denoting the z component of displacement on the upper wedge face (at $z = 0^-$) by $v(x, 0^-, t)$ and the *P*-, *S*- and Rayleigh-wave velocities by α, β, and γ, respectively, Miles' solution can be expressed as (for $t > x/\beta$)

$$v(x, 0^-, t) = A_1(\theta)\,\delta(t - x/\gamma) + A_2'(\theta), t)/\pi(t - x/\gamma), \tag{1}$$

where

$$A_1(\theta) = \frac{2\eta^2 - 1}{\alpha(1 + \eta)^{1/2}} \frac{\cos\theta(1 - \cos\theta)^{1/2}\,(1 + \nu\cos\theta)^{1/2}\,L(\eta)\,C(\theta)}{\xi - \cos\theta}, \tag{2}$$

$$A_2'(\theta, t) = \frac{(1 - 2\nu^2\cos^2\theta)(\alpha t/x - 1)^{1/2}\,L(\beta t/x)\,C(\theta)}{\beta(\alpha t/x - \cos\theta)}. \tag{3}$$

and

$$\eta = \beta/\gamma; \qquad \xi = \alpha/\gamma; \qquad \nu = \beta/\alpha, \tag{4}$$

$$C(\theta) = \frac{(1 + \cos\theta)^{1/2}\, L(-\nu\cos\theta)}{2\nu(1 - \nu^2)^{1/2}\,(\xi + \cos\theta)}, \tag{5}$$

$$L(z) = \exp\left\{\frac{1}{\pi}\int_{\nu}^{1} \mathrm{Tan}^{-1}\left[\frac{\zeta^2(1 - \zeta^2)^{1/2}\,(\zeta^2 - \nu^2)^{1/2}}{(\zeta^2 - \tfrac{1}{2})^2}\right]\frac{d\zeta}{\zeta - z}\right\}. \tag{6}$$

The expression for $A_2'(\theta, t)$ can be simplified by noting that all its time variation is small over the time duration of a pulse; that is, if we let $t = \tau + x/\gamma$, where $\tau = 0$ at the arrival time for *PcR*, we have

$$(\alpha t/x - 1)^{1/2} = (\xi - 1 + \alpha\tau/x)^{1/2} \approx (\xi - 1)^{1/2}, \tag{7}$$

$$\alpha t/x - \cos\theta = (\xi - \cos\theta + \alpha t/x) \approx \xi - \cos\theta, \tag{8}$$

$$L(\beta t/x) = L(\eta + \beta\tau/x) \approx L(\eta) \tag{9}$$

since all these three functions vary smoothly and little in value over the pulse duration ($\sim$7 μsec). Recall that $\eta = \beta/\gamma \approx 1.1$ while $\xi = \alpha/\gamma \approx 1.9$ and, for $x = a = 15$ cm, $x/\alpha \approx 27$ μsec and $x/\beta \approx 46$ μsec; therefore, over the duration of the pulse ($0 < \tau < 7$ μsec) we have $0 < \alpha\tau/x < 0.26$ and $0 < \beta\tau/x < 0.14$. Using the above approximations, we have

$$A_2'(\theta, t) \approx A_2(\theta) = (\xi - 1)^{1/2}\,(1 - 2\nu^2\cos^2\theta)\, D(\theta)/\beta, \tag{10}$$

$$A_1(\theta) = (2\eta^2 - 1)\cos\theta(1 - \cos\theta)^{1/2}(1 + \nu\cos\theta)^{1/2}/\alpha(1 + \eta)^{1/2}, \tag{11}$$

where

$$D(\theta) = (1 + \cos\theta)^{1/2}\, L(\eta)L(-\nu\cos\theta)/2\nu(1 - \nu^2)^{1/2}(\xi^2 - \cos^2\theta). \tag{12}$$

Using these expressions and the reduced travel time, τ, we have

$$v(x, 0^-, \tau) \approx A_1(\theta)\delta(\tau) + A_2(\theta)/\pi\tau \tag{13}$$

for times near the arrival of *PcR*. The amplitude of the wave does not vary with distance, as we would expect for a plane Rayleigh wave, and there are two components to the converted wave. The first component represents a reproduction in time of the incident *P*-wave waveform while the second represents a distortion of it. The latter time function, $1/\pi\tau$, is the *associated function* or the Hilbert transform of the delta function.

Figure 10 illustrates the distortion introduced by the presence of various amounts of the associated function. The top left waveform is the original function used to represent the experimental pulse. It is the second derivative of the Gaussian function, $50\exp(-t^2/100)$, or

$$f(t) = [0.02t^2 - 1]\exp(-t^2/100). \tag{14}$$

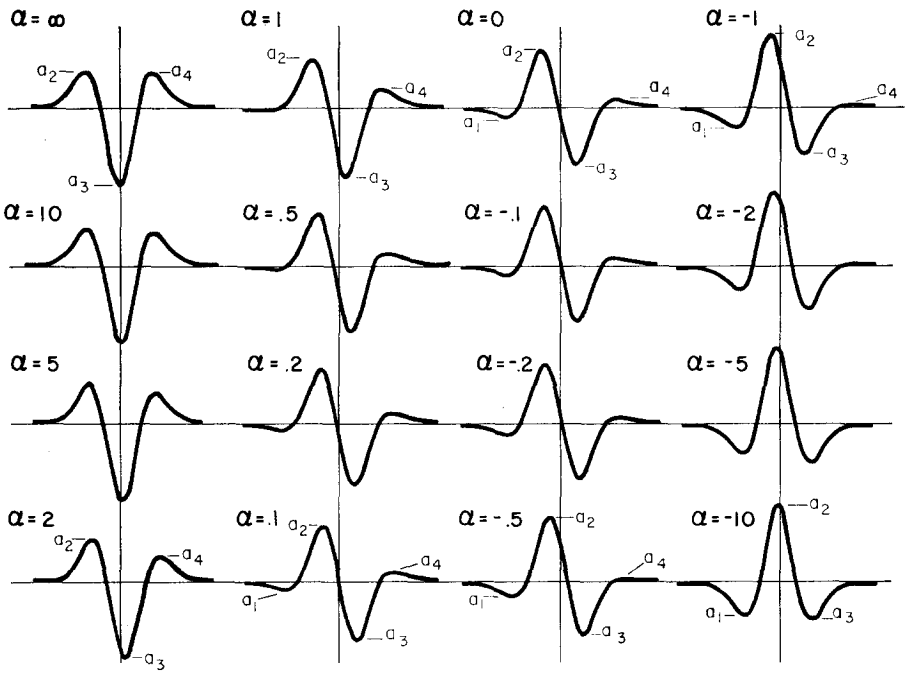

FIG. 10. The waveforms, $F(t)$, due to combining different ratios of the function $f(t)$ and its associated function $g(t)$; $F(t) = [\alpha f(t) + g(t)]/(1 + \alpha^2)^{1/2}$.

The remaining waveforms are given by

$$F(t) = [\alpha f(t) + g(t)]/(1 + \alpha^2)^{1/2}, \tag{15}$$

where

$$g(t) = f(t) * 1/\pi t \tag{16}$$

and the asterisk represents a convolution [31]. In performing the convolution numerically, the singular behavior of $h(t) = 1/\pi t$ at $t = 0$ must be taken into account. Analysis shows that the sampled version of $\pi h(t)$ has the values -0.75, 0, $+0.75$ at the sample values -1, 0, $+1$, respectively; the remaining values are obtained from $1/t$. Smoothed representations of the sampled functions for $f(t)$, $\pi h(t)$ and their convolution, $\pi g(t)$, are shown in Fig. 3. From this figure it is seen that convolution with $h(t)$ produces a great deal of distortion and the resulting waveform looks somewhat like the negative derivative of the original waveform. However, $g(t)$ has more low-frequency content and less high-frequency content than the derivative of $f(t)$. In Fig. 10, the waveform for $\alpha = 0$ corresponds to the function $g(t)$ and the waveforms go smoothly from $f(t)$ to $g(t)$ to $-f(t)$ as α is varied from $+\infty$ to 0 to $-\infty$.

The amplitudes of these waveforms (labeled a_1, a_2, a_3, and a_4) have been determined and their values are given in Table I. They have been normalized to the major lobe of the Gaussian function and they will be used to compare the theoretical and

TABLE I

Amplitudes as a Function of the Ratio $\alpha = A_1/A_2$ (See Fig. 10)

α	a_1	a_2	a_3	a_4
∞	−0.000	0.445	−1.000	0.445
10.0	−0.002	0.471	−0.995	0.419
5.0	−0.004	0.491	−0.990	0.396
2.0	−0.015	0.549	−0.958	0.326
1.0	−0.033	0.608	−0.902	0.246
0.5	−0.058	0.661	−0.832	0.178
0.2	−0.083	0.703	−0.774	0.133
0.1	−0.094	0.714	−0.752	0.118
0.0	−0.106	0.736	−0.736	0.106
−0.1	−0.118	0.752	−0.714	0.094
−0.2	−0.133	0.774	−0.703	0.083
−0.5	−0.178	0.832	−0.661	0.058
−1.0	−0.246	0.902	−0.608	0.033
−2.0	−0.326	0.958	−0.549	0.015
−5.0	−0.396	0.990	−0.491	0.004
−10.0	−0.419	0.995	−0.471	0.002
$-\infty$	−0.445	1.000	−0.445	0.000

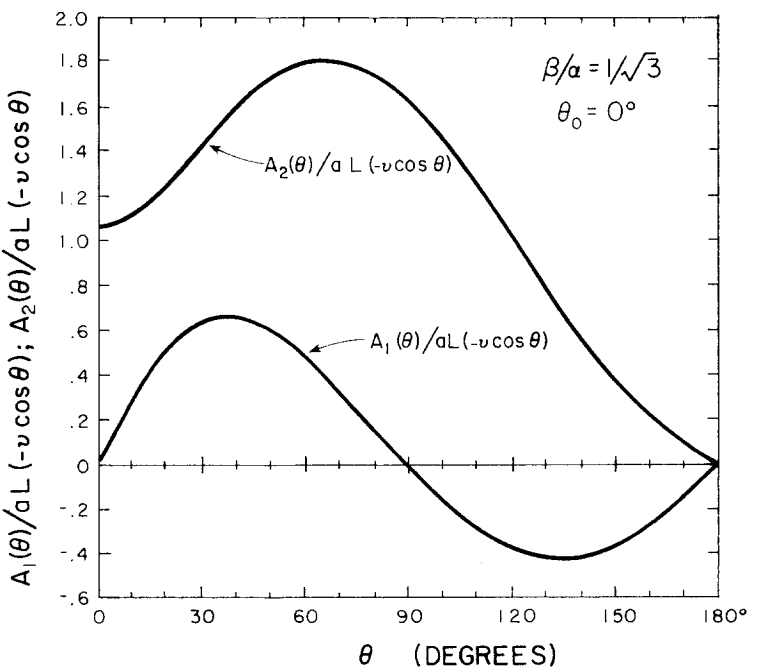

FIG. 11. The theoretical normalized coefficients, $A_1(\theta)/aL(-\nu\cos\theta)$ and $A_2(\theta)/aL(-\nu\cos\theta)$, of the input waveform and its associated function, respectively, for the *PcR* wave in the half-plane problem.

experimental results. The symmetrical character of these amplitudes is due to the symmetry of the originally assumed waveform.

The coefficients $A_1(\theta)$ and $A_2(\theta)$, normalized to a constant times $L(-\nu \cos \theta)$, are plotted in Fig. 11 for $0 \leqslant \theta \leqslant 180°$ and Poisson's ratio equal to 0.25. This shows that different ratios of the original waveform and its associated function occur as the angle θ is varied. A change in waveform as a function of θ is noted in the experimental data. Figure 12 shows tracings of the experimental traces for incidence angles, θ, of

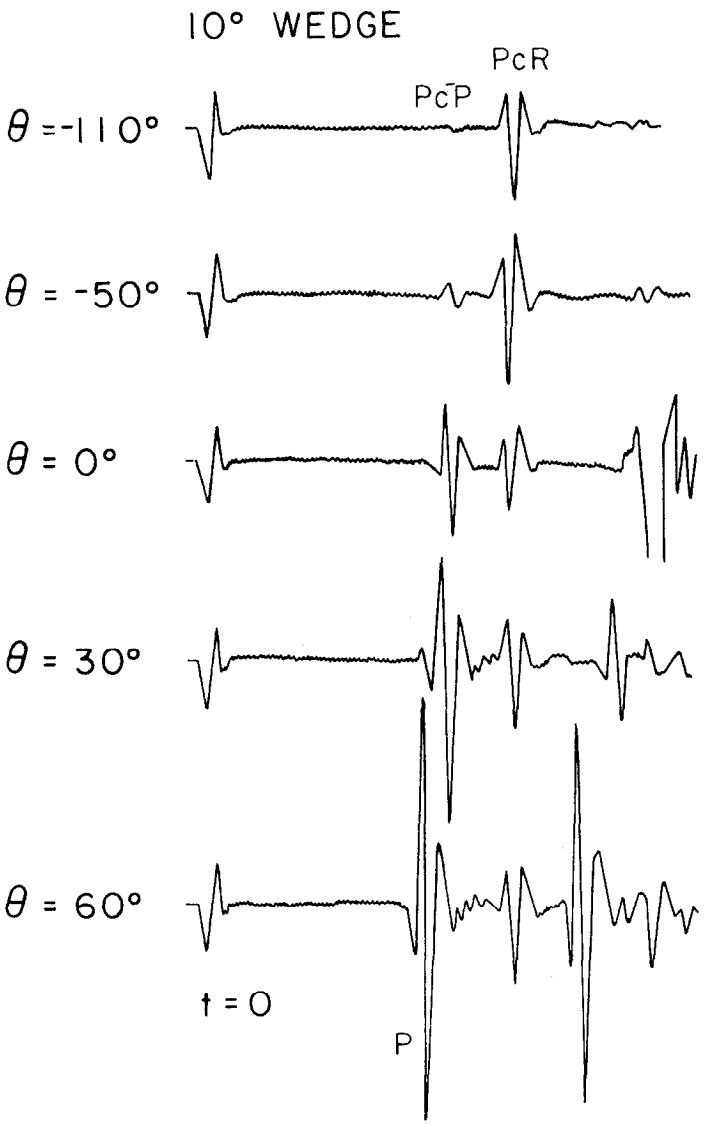

FIG. 12. Tracing of representative traces obtained from the seismic model for the 10° wedge.

-110, -50, 0, 30, and 60°. The change is particularly pronounced at $\theta = 30°$, near where the theory predicts the largest ratio of $A_1(\theta)/A_2(\theta)$ for $\theta < 120°$. These traces also show that the experimentally obtained waveform is similar to the assumed waveform, $f(t)$.

Note that the waveform of the direct P wave, which is clearly seen in the traces for $\theta = 30$ and 60°, is almost identical to the associated function of the PcR waveform in the traces for $\theta = 0$, 60, and $-50°$. This is due to the fact that PcR has a waveform similar to the second derivative of the Gaussian function and it is mainly composed of the associated-function component of the P wave. This is consistent with the theory because the associated function of an associated function is the negative of the original function; in other words, the Hilbert transform of a Hilbert transform gives the negative of the original function [31]. Another way of saying the same thing is that the convolution of $1/\pi\tau$ with itself is equal to the negative of the delta function, $\delta(\tau)$,

$$1/\pi\tau * 1/\pi\tau = -\delta(\tau). \tag{17}$$

Apparently, the transducer emits a P-wave pulse whose waveform is similar to the associated function of the second derivative of a Gaussian function.

Miles' expressions for $v(x, o^-, t)$ are valid only for incidence angles, θ, lying between 0 and 90° (and, by symmetry, between 0 and $-90°$). We have plotted the values for $A_1(\theta)$ and $A_2(\theta)$ over the full range of θ even though there may be some changes required for $\theta > 90°$. For example, a simple review of Miles' analysis indicates that the negative values of $A_1(\theta)$ for $\theta > 90°$ should be positive. There is some indication in the experimental data that this is the case (see Fig. 4). The function $L(-\nu \cos\theta)$ was not included in the curves for $A_1(\theta)$ and $A_2(\theta)$ in Fig. 11 because of its complex nature. The integral, ln $L(z)$, has been evaluated by Gaussian integration [32] using 4 through 16 point formulas. It was found that a 12 point Gaussian integration is

0.707 and the other from 0.707 to 1, and different transformations are used in each interval. The change in variable used in the first interval is $(\zeta - \nu)^{1/2}$ and that used in the second interval is $(1 - \zeta)^{1/2}$. These transformations are required because Gaussian integration gives accurate results if the integrand can be closely approximated by polynomials; that is, the integrand should have continuous high-order derivatives over the integration interval. The above two transformations eliminate the infinite first derivatives of the inverse-tangent function at the two limits of integration, ν and 1.

Representative values of $L(z)$ are given in Table II for $-3^{-1/2} \leqslant z \leqslant 3^{-1/2}$ which corresponds to $0 \leqslant \theta \leqslant 180°$. It can be seen that $L(z)$ is fairly constant for $-3^{-1/2} \leqslant z \leqslant 0$ (or $0 \leqslant \theta \leqslant 90°$) and varies rapidly only for $z > 0.8(3^{-1/2})$ (or $\theta > 145°$). Its most rapid variation occurs near $z = 3^{-1/2}$ (or $\theta = 180°$) and it has its maximum value there. However, note the value is finite (8.9656) and not infinite as indicated by Miles [8, Fig. 9, p. 51]. Because of the behavior of $L(-\nu \cos\theta)$, the curves for $A_1(\theta)$ and $A_2(\theta)$ should give a good representation for the amplitude variation of PcR for angles between $\pm 90°$ and, if the extension of Miles' equation is valid, for angles

TABLE II

Values of $L(z) = L(-\nu \cos \theta)$, $\nu = 1/3^{1/2}$

$z/3^{1/2}$	θ (deg)	$L(z)$
−1.0	0	1.1373
−0.8	36.9	1.1512
−0.6	53.1	1.1684
−0.4	66.4	1.1900
−0.2	78.5	1.2180
0	90.0	1.2559
0.2	101.5	1.3101
0.4	113.6	1.3942
0.6	126.9	1.5442
0.8	143.1	1.9006
0.82	145.1	1.9669
0.84	147.1	2.0450
0.86	149.3	2.1385
0.90	154.2	2.3978
0.92	156.9	2.5881
0.94	160.1	2.8536
0.95	161.8	3.0328
0.96	163.7	3.2624
0.97	165.9	3.5727
0.98	168.5	4.0305
0.99	171.9	4.8365
1.00	180.0	8.9656

between $\pm 145°$. The rapid variation of $L(-\nu \cos \theta)$ at $\theta = 180°$ means the amplitude of *PcR* would be larger than predicted by $A_1(\theta)$ and $A_2(\theta)$, but would still be zero at 180° because of the finite value of $L(-\nu \cos \theta)$ there. A zero amplitude for *PcR* was not measured at the wedge edge (at −170°) which should correspond to $\theta = 180°$ for the half-plane problem. This may be due to two reasons. (i) The theoretical values are for a wedge angle of 0° while the experimental values were obtained for a wedge angle of 10°; however, it would be surprising if this small a change in angle makes that much difference. (ii) The receiving transducer has finite size and measures amplitudes from a small range of angles, approximately 0.5°, about the nominal value. The rapid increase in amplitude from 0 at −180° to finite values at smaller negative angles could account for the nonzero measured value. The function $L(-\nu \cos \theta)$ produces the rapid increase in *PcR* for the source located near the wedge face (i.e., for $\theta \simeq -170$ and $+180°$).

The sum of the peak-to-peak amplitudes $(a_2 - a_3 + a_4 - a_3)$ in Fig. 10 gives values that vary only between 2.89 and 2.50 for amplitude ratios, α, between ∞ and 0.5. This covers most of the range of amplitude ratios shown in Fig. 11, at least for angles between $\pm 170°$. Therefore, over this range, the measured amplitude should vary approximately as $[A_1^2(\theta) + A_2^2(\theta)]^{1/2} L(-\nu \cos \theta)$. Values of this latter quantity,

TABLE III

Theoretical Amplitudes for 0° wedge Normalized to 60°

$$A = \frac{[A_1^2(\theta) + A_2^2(\theta)]^{1/2} L(-\nu \cos \theta)}{[A_1^2(60°) + A_2^2(60°)]^{1/2} L(-\nu \cos 60°)}$$

θ (deg)	A
0	0.56
15	0.65
30	0.81
45	0.95
60	1.00
75	0.98
90	0.93
105	0.84
120	0.73
135	0.59
140	0.58
145	0.56
150	0.50
155	0.48
160	0.45
165	0.42
170	0.35
175	0.25
180	0.00

normalized to one at 60°, are given in Table III. These points have been plotted in Fig. 4 with the data for the 10° wedge angle. There is excellent correlation of the theoretical and measured values, especially considering that the theoretical values are for a 0° wedge. There is some asymmetry in the 10° wedge data and a better fit of the two sets of data would be obtained if the theoretical data were shifted +5°, corresponding to the line of symmetry for the model, and if the range of the theoretical data was contracted to ±175° from ±180°. Considering the approximate nature of the comparison, it was not felt that these latter two "refinements" of the theoretical data were justified. In particular, there appears to be a small cusp in the experimental data near −140° which does not have a counterpart in the theoretical data. This cusp may be due to experimental error; on the other hand, the theoretical results for a 10° wedge might show the same feature.

Summary and Conclusions

Experimental measurements of the amplitudes of *PcR* as a function of the incidence angle, θ, of the *P* wave have been obtained from two-dimensional seismic models for wedge angles $\theta_0 = 10, 30, 60, 90$, and 120°. The measured values show the follow-

ing characteristics. (i) The *PcR* amplitudes show a minimum near $\theta = 0°$ (the incident *P* ray is parallel to the upper wedge face), minima at $\theta = \theta_0 - 180°$ and at 180° (the latter is inferred from the data), and maxima near $\theta = \pm 90°$. These results are consistent with those measured earlier [28] for $\theta_0 = 60$ and 90°. (ii) The amplitudes of *PcR* decrease as the wedge angle increases to 120°. This is consistent with the fact that the amplitudes of *PcR* must be identically zero for all angles of θ for $\theta_0 = 180°$; that is, for a half space. (iii) The *PcR* amplitudes become less symmetric about $\theta = 0$ as the wedge angle increases.

The *PcR* amplitudes, observed on the top wedge face and due to *P* waves incident on the wedge tip, should be identical to the *RcP* amplitudes observed on the circular periphery of the model for a source of Rayleigh waves on the upper wedge face. This is a direct consequence of the principle of seismic reciprocity [33, 34].

The experimental data for the 10° wedge have been compared with the theoretical results for the 0° wedge and very good correlation is observed, generally they are the same within ± 10 %. Considering the experimental error, about ± 5 %, and the fact that the theory is for a slightly different case, this is surprisingly good agreement.

The converted wave, *PcR*, has two components; one is a reproduction of the incident *P* wave and the other is its associated function or Hilbert transform. The ratio of the amplitudes of these two components vary as the incidence angle is varied and this causes a change in wave shape for *PcR* as a function of θ. This waveform variation is found to exist in the experimental data and appears to have the largest effect near 30° (for the $\theta_0 = 10°$ case) and this is where the theory predicts a large variation.

In addition, it is noted that the major component of the *PcR* wave is the associated-function one, both according to the theory for the 0° wedge and according to the measured waveform of the direct *P* wave in the 10° wedge case.

No correlation of the experimental data with numerical, finite-difference solutions of these problems was made because there are not sufficient or adequate data to make one. It is hoped that presenting these experimental data will encourage numerical analysts to treat these problems in greater detail.

REFERENCES

1. H. LAMB, *Phil. Trans. Roy. Soc. London Ser. A* **203** (1904), 1–42.
2. M. M. FRIDMAN, *Dokl. Akad. Nauk SSSR* **60** (1948), 1145–1148.
3. M. M. FRIDMAN, *Dokl. Akad. Nauk SSSR* **66** (1949), 21–24.
4. A. W. MAUE, *Z. Angew. Math. Mech.* **33** (1953), 1–10.
5. M. ROSEAU, *Compt. Rend.* **245** (1957), 1888–1890.
6. M. ROSEAU, *Comm. Pure Appl. Math.* **12** (1959), 67–85.
7. A. T. DE HOOP, "Representation Theorems for the Displacement in an Elastic Solid and their Application to Elastodynamics Theory," Sc.D. thesis, Technische Hogeschool, Delft, 1958.
8. J. W. MILES, *Quart. Appl. Math.* **18** (1960), 37–59.
9. E. R. LAPWOOD, *Geophys. J. Roy. Astron. Soc.* **4** (1961), 174–196.
10. K. VISWANATHAN, J. T. KUO AND E. R. LAPWOOD, *Geophys. J. Roy. Astron. Soc.* **24** (1971), 401–414.

11. J. KANE AND J. SPENCE, *Geophysics* **28** (1963), 715–723.
12. J. A. HUDSON AND L. KNOPOFF, *J. Geophys. Res.* **69** (1964), 281–289.
13. A. K. MAL AND L. KNOPOFF, *Bull. Seismol. Soc. Amer.* **56** (1966), 455–466.
14. A. MCGARR AND L. E. ALSOP, *J. Geophys. Res.* **72** (1967), 2169–2180.
15. Z. S. ALTERMAN AND A. ROTENBERG, *Bull. Seismol. Soc. Amer.* **59** (1969), 347–368.
16. Z. S. ALTERMAN AND D. LOWENTHAL, *Geophys. J. Roy. Astron. Soc.* **20** (1970), 101–126.
17. M. OTTAVIANI, *Bull. Seismol. Soc. Amer.* **61** (1971), 1119–1152.
18. M. MUSASINGHE AND G. W. FARNELL, *J. Geophys. Res.* **78** (1973), 2454–2466.
19. A. K. MAL AND L. KNOPOFF, *Bull. Seismol. Soc. Amer.* **55** (1965), 319–334.
20. J. CL. DEBREMAECKER, *Geophysics* **23** (1958), 253–266.
21. I. A. VICTOROV, *Sov. Phys. Dokl.* **3** (1958), 304–306.
22. L. KNOPOFF AND A. F. GANGI, *Geophysics* **25** (1960), 1203–1214.
23. A. F. GANGI, "Elastic Waves in Wedges," Ph.D. thesis, University of California, Los Angeles, 1960.
24. W. L. PILANT, L. KNOPOFF, AND F. SCHWAB, *J. Geophys. Res.* **69** (1964), 291–297.
25. D. LEWIS AND J. W. DALLY, *J. Geophys. Res.* **75** (1970), 3387–3398.
26. A. N. HENZI AND J. W. DALLY, *Geophysics* **36** (1971), 296–310.
27. J. W. DALLY AND D. LEWIS, *Bull. Seismol. Soc. Amer.* **58** (1968), 539–563.
28. A. F. GANGI, *J. Geophys. Res.* **72** (1967), 5685–5692.
29. R. L. WESSON, "Experimental Determination of Rayleigh/P-Wave Conversions at Corners," B.S. thesis, Massachusetts Institute of Technology, Cambridge, 1966.
30. J. OLIVER, F. PRESS, AND M. EWING, *Geophysics* **19** (1954), 202–219.
31. R. BRACEWELL, "The Fourier Transform and Its Applications," McGraw–Hill, New York, 1965.
32. M. ABRAMOWITZ AND I. A. STEGUN, "Handbook of Mathematical Functions," Applied Math Series, 55, U.S. Dept. of Commerce, N.B.S., U.S. Govt. Printing Office, Washington, D.C., 1964.
33. L. KNOPOFF AND A. F. GANGI, *Geophysics*, **24** (1959), 681–691.
34. D. GRAFFI, *Mem. Acad. Sci. Bologna, Ser.* **10**, **4** (1946), 103–108.